Research Article

Functionalization of Carbon Electrodes with Nanotitania by Atomic Layer Deposition

Graciano B. De Souza [1,2] **Dachamir Hotza** [1] **Rolf Janßen** [3] **Kaline P. Furlan** [3] and **Carlos R. Rambo** [1,2]

[1]*Graduate Program in Materials Science and Engineering, Department of Mechanical Engineering, Federal University of Santa Catarina, Florianopolis 88040-900, Santa Catarina, Brazil*
[2]*Laboratory of Electrical Materials, Department of Electrical and Electronic Engineering, Federal University of Santa Catarina, Florianopolis 88040-900, Santa Catarina, Brazil*
[3]*Institute of Advanced Ceramics, Integrated Materials Systems Group, Hamburg University of Technology (TUHH), Denickerstraße 15 21073, Hamburg, Germany*

Correspondence should be addressed to
Carlos R. Rambo; carlos.rambo@ufsc.br

Carbon fibers are materials with a very high surface area and are interesting for applications such as filters, fire-resistant heat insulation, photocatalysis, and capacitor electrodes. Moreover, thermal burnout can easily remove these fibers, making them ideal templates for high-precision coatings or keeping them within the coated structure, generating nanostructured composites. In this work, two different substrates, carbon felt and bacterial nanocellulose were coated by TiO_2 with atomic layer deposition (ALD). After deposition, the templates were pyrolyzed or further removed by burnout in the air. The microstructure evolution of the 3D interlocked-fibers structures was characterized by scanning electron microscopy and nitrogen adsorption surface area after each step. Stable anatase was present as a single TiO_2 phase even after heat treatment at 800°C. Moreover, electrochemical impedance spectroscopy and constant current charge-discharge were employed to investigate the electrochemical properties of the samples. Our results show that all samples display a uniform layer after ALD and that the surface area decreases with an increasing number of ALD cycles. After burnout, the 3D structures presented a straw-like appearance to the shells. Nonetheless, both samples presented a power density comparable to a porous NiO/C, with the pyrolyzed bacterial nanocellulose sample displaying a higher pseudocapacitance performance than the carbon-felt samples.

1. Introduction

Atomic layer deposition (ALD) is a thin film deposition technique that exposes the surface separately to at least two different gaseous molecules, the precursor and the co-reactant, so that a thin layer is formed from the reaction between the surface and each gas [1]. Self-limiting surface-controlled reactions enable very precise and molecular scale control of layer thickness [2] and the possibility of coating substrates with very high aspect-ratios and complex 3D structures with very high aspect ratios [1, 3]. ALD has come a

long way since its early days when it was still called atomic layer epitaxy [4]. Several studies have been conducted on ALD coating fibers for various applications [z5]. The application of TiO_2 ALD as a photocatalytic is plausible due to the physicochemical properties of titania and the possibility of its coupling with other semiconductors [6, 7], while Al_2O_3 is for its hydrophobicity [8, 9].

The capacity of ALD to form a controlled thin film, even on very porous and intricate structures, has already been demonstrated before. For example, Furlan et al. demonstrated that alpha-Al_2O_3 ALD can be applied to microsized

polymer particles to create a highly porous inverse opal structure with large domains of identical crystalline orientation. These structures provide greater thermal stability and may be used in filters [10].

There are several studies on ALD deposition temperature, as it is a key processing factor and varies a lot depending on the precursor composition. Zhu et al. investigated the effects of deposition temperature and the effect of film thickness on the crystallographic state. They have found that below 165°C the process tends to favor chemical reactions rather than surface adsorption, generating a CVD process in which the thickness is not finely controlled as in usual ALD. At higher temperatures, they were able to deposit thin (>40 nm) films of SnO_2 on carbon nanotubes and test them as anodes, finding a high specific capacitance [11]. This is in contrast to titanium isopropoxide which can be deposited at 95°C [12].

Recent work has also carried out explorations regarding the number of ALD cycles. Gakis et al. showed that the progression of the very first ALD cycles (<25) of Al_2O_3 on an H-terminated Si (100) substrate can be modeled with the geometric growth aspects, disregarding the changes in surface reactivity. This growth model is significant for understanding and controlling very thin films [13].

Cao et al. described how they produced a highly electrochemically stable nanolaminate anode for lithium-ion batteries using ALD. The group deposited ZnO and TiO_2 alternatively on a copper foil through 24 full cycles, comprising 26 half cycles for each oxide. They found a charge capacity of more than 600 mAh/g [14]. In 2020, Cao et al. and their collegues demonstrated that it is possible to achieve a high photocatalytic activity under visible light by depositing Fe_2O_3 via ALD on commercially available TiO_2 powder with only 400 cycles. They managed to obtain over 95% methyl orange degradation in 90 min [15]. This leads to the consideration that cycles in the thousands, or lower, frequency range might be optimal for achieving some electrochemical proprieties without creating an effective metal oxide insulation barrier.

The morphology of the substrate, such as porosity, tortuosity, etc., can affect the final deposited layer microstructure. This has been demonstrated by Trought et al. They used different morphologies and densities of functional sites, produced by etching a carbon substrate (highly oriented pyrolytic graphite) with different acids, to show that these two variables can affect the nucleation of deposited Al_2O_3 deposited through ALD [16].

However, ALD is not restricted to ceramic or metallic substrates. There are studies on atomic layer deposition employed over polymeric materials. An et al. have thoroughly reviewed the process of supersonic spraying at near ambient temperature, including the coating of polymeric nanofibers with reduced graphene oxide, which can be tuned for many applications such as sensors and water-based photoelectrodes [17]. While Darwish et al. successfully coated poly (methyl methacrylate) (PMMA) through ALD at a low temperature (65°C) with a thin film of TiO_2 and achieved a water contact angle 90% lower than the uncoated PMMA [18].

Among the wide variety of polymers, bacterial nanocellulose (BNC) is known for its 3D structure composed of high-purity cellulose fibers. For some microorganisms, these natural polymer fibers work as a mechanical shield from the environment and are synthesized by specific bacteria. These fibers are nanometric and are arranged in a way that at the same time avoids dehydration but allows the flow of nutrients to the bacteria. The geometry of this porous body can be easily adjusted to a variety of shapes simply by changing the culture medium container, eliminating the need for postprocessing [19].

In a recent review of the production process of BNC, Parte et al. discuss some different bioreactor shapes and agitation methods together with their BNC shape results. It is a highly valuable review of the growth limitations, parameters, and media of BNCs, useful for large-scale industrial production [20].

In 2008, Rühs et al. indicated a direct method for producing three-dimensional BNC with controlled macroporosity by foaming the medium with mannitol accompanied by a stabilizer (Cremodan) and a viscosity tuner (Xanthan) [21].

A general review and some new findings in the major fields of BNC, biomedicine, and biotechnology are presented by Swingler et al. Despite the recognizable biocompatibility of BNC, only a few studies have been conducted in humans (*in vivo*) [22], though with promising results for recovering the depth of ulcers [23]. Another study was an attempt to restore the tympanic membrane (eardrum) using a BNC patch [24].

In 2019, Gao et al. demonstrated a technique for growing, using functionalized glucose under the method of *in situ* microbial fermentation, a fluorescence BNC confirming that BNC (K. sucrofermentans) can metabolize modified glucose [25].

One of the differences between depositing on a nonwoven pyrolyzed fiber and the nanocellulose is the reactive groups at the surface. As explained by Norrrahim et al., BNC has a high concentration of hydroxyl groups(-OH) that enables easy functionalization of nanocellulose [26]. Kynol fibers are pyrolyzed at high temperatures (>700°C) and during this process hydroxyl and methylol groups and noncyclic groups are lost. These Kynol carbon fibers contain proportionally less hydrogen and oxygen, as low as 5% in weight [27], when compared to bacterial nanocellulose, which has around 55% of hydrogen and oxygen in weight, or 5 OH per nm^2 [28]. That is one of the reasons why BNCs are effectively more reactive and very attractive for the ALD process.

Applying ALD to nanocellulose is, however, not new. In 2014 Habibi reported a summary of the advances in the chemical modification of nanocellulose [29]. In an efficient review of nanocellulose oil sorbents, Liu et al. include ALD as a commonly used hydrophobization process of cellulose-based aerogels [30]. It has also been found that BNC coated with aluminum oxide via ALD may present excellent sorption of fluoride ions, with maximum adsorption of fluorine at only 50 nm layer thickness [31].

Among several applications, ALD-coated BNC-derived carbon aerogels can be used as lightweight capacitor
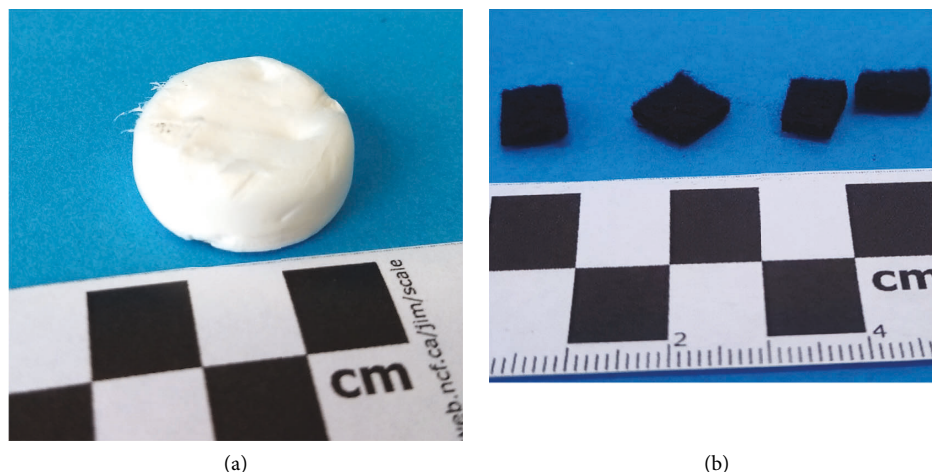
(a)   (b)

FIGURE 1: In (a) BNC sample after supercritical drying. (b) Kynol nonwoven samples are cut into 1×1 cm pieces.

electrodes. The main advantage of capacitors is their ability to deliver electrical energy, previously stored, at speeds much greater than those of conventional batteries. This delivery occurs through an applied potential to two plates (electrodes), separated by a dielectric material, on which the electrical charges will accumulate. In the case of electrochemical capacitors, the ions of an electrolyte solution will flow to one plate or the other, depending on their charge [32]. Carbon is one of the most commonly used materials as an electrode in electrochemical capacitors because it meets the requisites of good conductivity and electrochemical stability [32, 33]. However, what will distinguish the different forms of carbon, and thus their electrochemical properties, are two key characteristics: specific surface area (SSA) and open porosity [33]. These two characteristics are both present in BNC.

Several studies have applied ALD on mesoporous substrates [34, 35], in special carbon ones; however, most of them start off with carbon-ready substrate sor nonbacterial cellulose. We aim to process pyrolysis and heat treatment simultaneously, similar to the approach of Ma et al. [36]. This paper explores, therefore, BNC, a natural polymer, and nonwoven carbon (Kynol), two 3D interlocked fibers' structures, as a carbon source when subjected to atomic layer deposited titanium oxide, with potential application as electrodes for capacitors.

2. Materials and Methods

2.1. Samples Preparation and Functionalization. Bacterial nanocellulose (BNC) thick membranes were synthesized by the bacteria *Gluconacetobacter xylinus*, following the procedure described in [37]. Briefly, the bacteria were grown inside a Falcon tube for several days until the hydrated nanocellulose layer had reached 1 cm in height. Next, the bacteria were removed from the formed 3D structure using NaOH (100 mM) at 50°C for 24 h, and the cellulose was rinsed with distilled water [37]. The nanocellulose hydrogel passed through a solvent exchange, from water to ethanol, consisting of 5 progressive exchanges over two days.

The ethanolic gel was then supercritically dried with three cycles of CO_2, using an Autosamdri 931 supercritical drier, which resulted in nanocellulose aerogels that maintained their structure as shown in Figure 1(a). These were then cut into small chunks of approximately 0.5×1.0 cm. These processing steps, namely supercritical drying, were combined with a pyrolysis step after the deposition, later described, to achieve a carbon structure comparable to the nonwoven activated carbon.

The second substrate was a highly porous and high specific surface area activated carbon (95%) nonwoven textile called ACN-211-20 (Kynol Europa GmbH) called Kynol. These commercial fibers are derived from a three-dimensional cross-linked phenolic resin [27]. The samples were cut into 1×1 cm pieces and used as received, without additional treatment, as seen in Figure 1(b).

Atomic layer deposition was carried out in a homemade reactor (Hamburg University of Technology, Institute of Advanced Ceramics – Integrated Materials Systems Group) under exposure mode at a low temperature of 95°C using nitrogen as the carrier gas. For the deposition, titanium oxide was chosen due to its electric properties as an electrode [38, 39], lower toxicity, and potential photocatalytic properties [4]. The precursor used was titanium isopropoxide (TTIP; Sigma-Aldrich) and deionized water as the coreactant. Both samples were subjected, separately, to two different ALD processes that comprised 350 or 700 cycles. Figure 2 shows the process scheme of the gas flow sequence in and out of the chamber, including the exposure time. TTIP and water pulse/exposure/purge time were 1/30/60 and 0.1/30/90 seconds, respectively.

Because of the samples' highly porous and low-density nature, a large mesh stainless steel dome was built within the chamber to protect the samples and avoid displacement during the pulse of the precursors. In each process, a total of 8–10 samples were placed in the reactor. A piece of a commercial silicon wafer (as received, <100>, Si-Mat silicon materials) was placed inside the chamber next to the samples to estimate the equivalent layer thickness after deposition. These silicon wafer pieces' layer thickness were analyzed
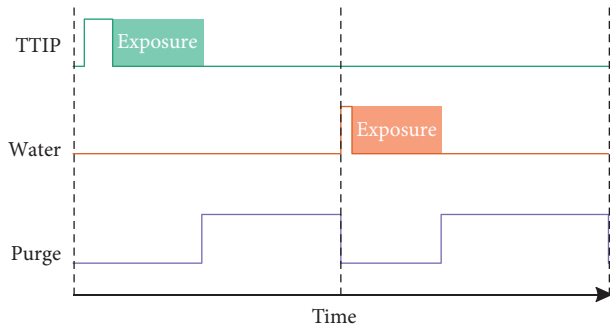
FIGURE 2: ALD time-step cycle plot with each precursor pulse, exposure, and purge steps over time.

using a spectroscopic ellipsometer (SE-2000, Semilab Semiconductor Physics Laboratory Co., Ltd.) using the Tauc-Lorentz dispersion law, with a wavelength range between 450.06 and 974.66 nm and an angle of incidence of 70.12°.

After the ALD deposition, the BNC aerogel was subjected to a pyrolysis process under an N_2 atmosphere, with a heating rate of 10°C/min until the plateau temperature of 800°C, which was held for two hours. A Kynol sample was burned in a muffle furnace using a heat rate of 10°C/min until the plateau temperature of 400°C, which was held for two hours for SEM inspection. The kynol samples used in the electrode assembly were not heat-treated.

2.2. Characterization.

To evaluate the microstructural evolution of the samples, scanning electron microscopy (SEM - Zeiss Supra VP 55) was used before and after each stage. The samples were analyzed in four different states: before and after deposition; after pyrolysis; and after burnout (template removal). The burned-out state was used to analyze the ALD coating in detail. After attaching the samples to a conductive carbon tape on an appropriate metal stub, they were subjected to a gold sputter deposition process with 40 mA for 30 seconds under argon flux.

The phases were characterized by X-ray diffraction (XRD) performed with a Rigaku MiniFlex X-ray diffractometer, using a copper source (λ K_α 1.540593 Å), with 10 deg/min, and a step time of 0.02 s. Phase identification was carried out with the QualX software (v2.24) and Profex (v4.3.5) [40, 41]. The anatase spectrum was refined using the Rietveld method. The carbon structure of the Kynol sample was further investigated by Raman spectroscopy with the innoRam (B&W TEK) spectrometer, using a 532 nm wavelength green laser. For the specific surface area (SSA) evaluation, the samples were first subjected to a vacuum degassing for two hours under 120°C to remove humidity and other adsorbed species. The nitrogen adsorption analysis using the Brunauer-Emmett-Teller (BET) method was carried out on a Quantachrome Nova 1200e equipment operated at 77 K, using 240 seconds as thermal equilibrium timeout.

The electrodes used for the electrochemical characterization were produced by coating an aluminium plate with a slurry of the active material sample (BNC or Kynol). In order to
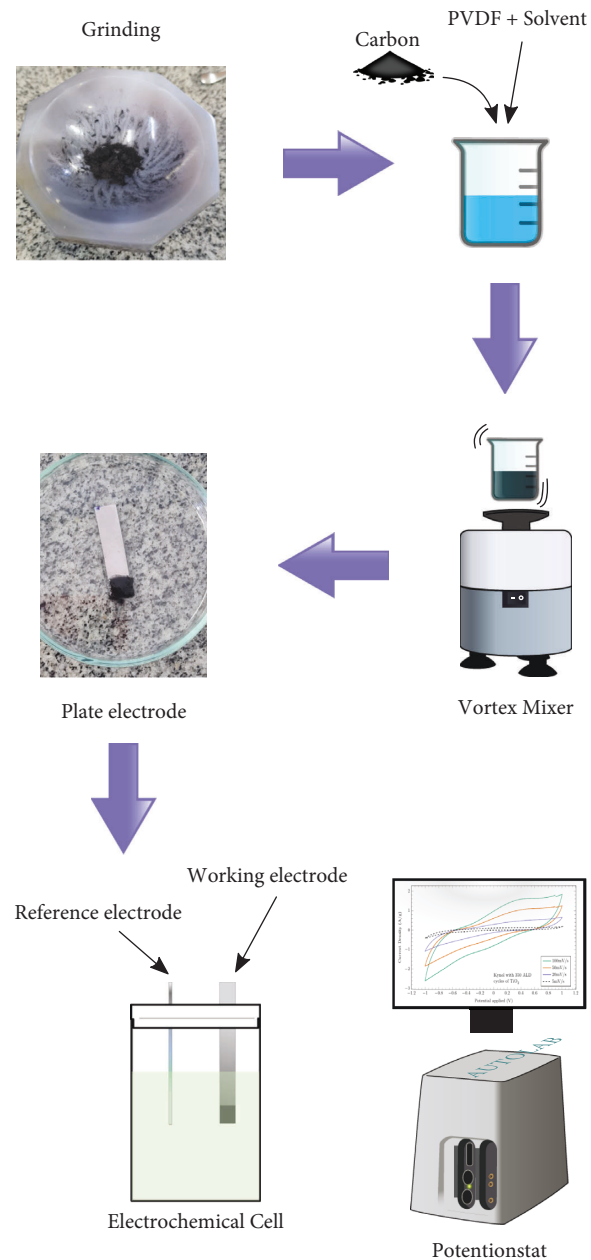

FIGURE 3: Schematic of the electrode assembly steps.

accomplish that, the samples were ground into a fine powder using an agate mortar and pestle, then added to a binder solution with the following *sample*: *binder*: *solvent* weight proportion of 10 : 1:1000 (carbon, PVDF, N-Methyl-2-pyrrolidone) and thoroughly mixed using a vortex vibrator. The prepared slurry was carefully applied to the aluminium plate with a spatula and then dried at 120°C for six hours. A simplified scheme of the electrode assembly is shown in Figure 3. Electrochemical properties were measured using a Metrohm potentiostat (Autolab PGSTAT204 FRA32 M) coupled with Nova 2.0 software. A two-electrode setup was employed for these measurements, with a high-purity Pt as a counter electrode in a 1 M KOH solution. Cyclic voltammetry curves (CV) were performed at scan rates between 5 and 100 mV/s, while impedance was measured between 100 kHz and 1 Hz.

TABLE 1: TiO$_2$ layer thickness on Si wafer through spectroscopic ellipsometry analyzer regression.

Sample run	Thickness (nm)	Fit (R^2)
BNC 700	17.8	0.98257
Kynol 700	21.4	0.9994

(a)

(b)

(c)

(d)
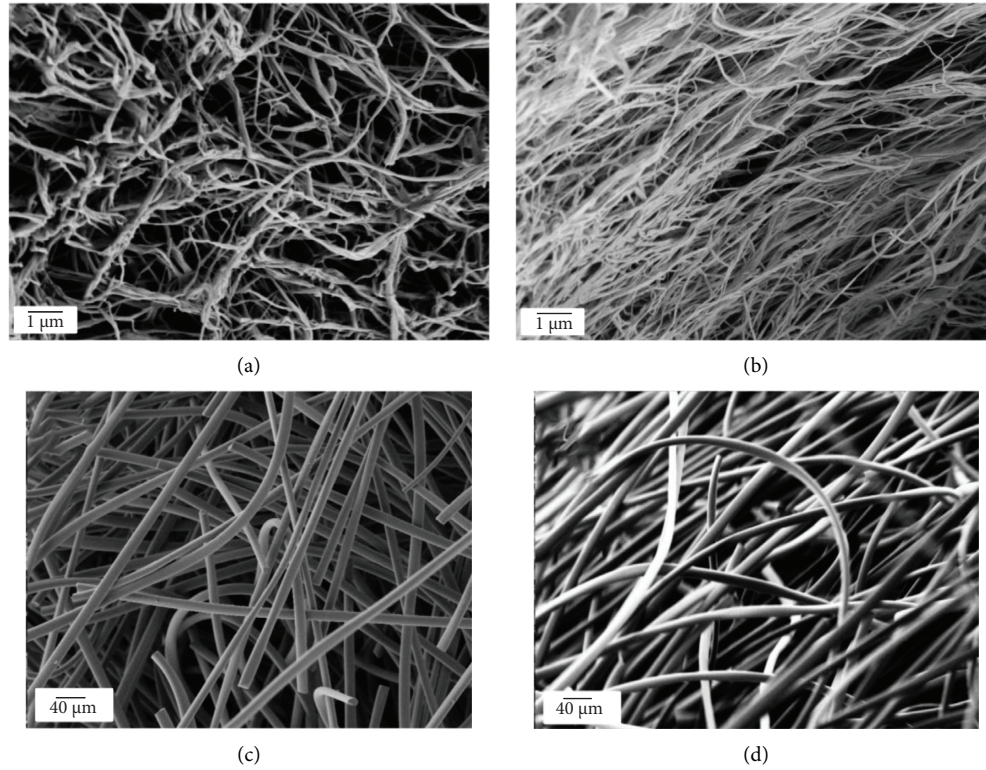
FIGURE 4: Comparison between the morphology of nanocellulose samples in (a) uncoated and (b) after TiO$_2$ coating by ALD, in (c) Kynol uncoated fiber, and (d) Kynol after TiO$_2$ coating.

The specific capacitance (C_p) was calculated from the area of the CV curves using

$$C_p = \frac{A}{2km\Delta V},\qquad(1)$$

where A is the integrated area from the voltammetry curve, k is the voltage sweep rate, m is the mass of the electrode, and ΔV is the voltage range.

3. Results and Discussion

3.1. Ellipsometry. In order to allow us to evaluate the performance of the ALD process itself, we measured the TiO$_2$ layer thickness indirectly, on the silicon wafer pieces, as displayed in Table 1. These results indicate that the deposition occurred normally. Our findings are very close to those found by Skopin et al. for 2 seconds exposure of titania deposition on silicon substrate [42].

3.2. Microstructural Characterization. Scanning electron micrographs (SEM) of the kynol and nanocellulose samples are shown in Figure 4, where the original morphology of the fibers is preserved after ALD with titania. In Figure 4(a) (25 k magnification) the bacterial nanocellulose fibers appears entangled, branching into various directions, and several nanometers distant from one another, similar to previous studies [25, 43]. In Figure 4(c) (500X magnification) the Kynol fibers display a more straight pattern, also equally far apart from each other, resembling the findings of Lee [44]. As expected from ALD processing, no defects were identified in the coatings (Figure 4(b) and 4(d)), indicating a uniform layer.

In Figure 5 presents SEM and particular zoomed images of the samples after pyrolysis (in nitrogen), or burnout (in the air), show that all samples are still highly porous, even though morphological alterations are present. For the nanocellulose-pyrolyzed samples (Figure 5(a) and 5(b)), sintering of the fibers is observed, with the formation of spider-net-like structures. Previous publications by our group [12] on ALD-based TiO$_2$ inverse opals with nanometric features have shown that sintering is quite pronounced for such nanostructures, leading to complete destabilization and the formation of a vermicular structure after 900°C [45].

For Kynol samples (Figures 5(c) and 5(d)), heat treated in air, a squished straw-like tubular shape is observed also with enlargement compared to the dimensions of the
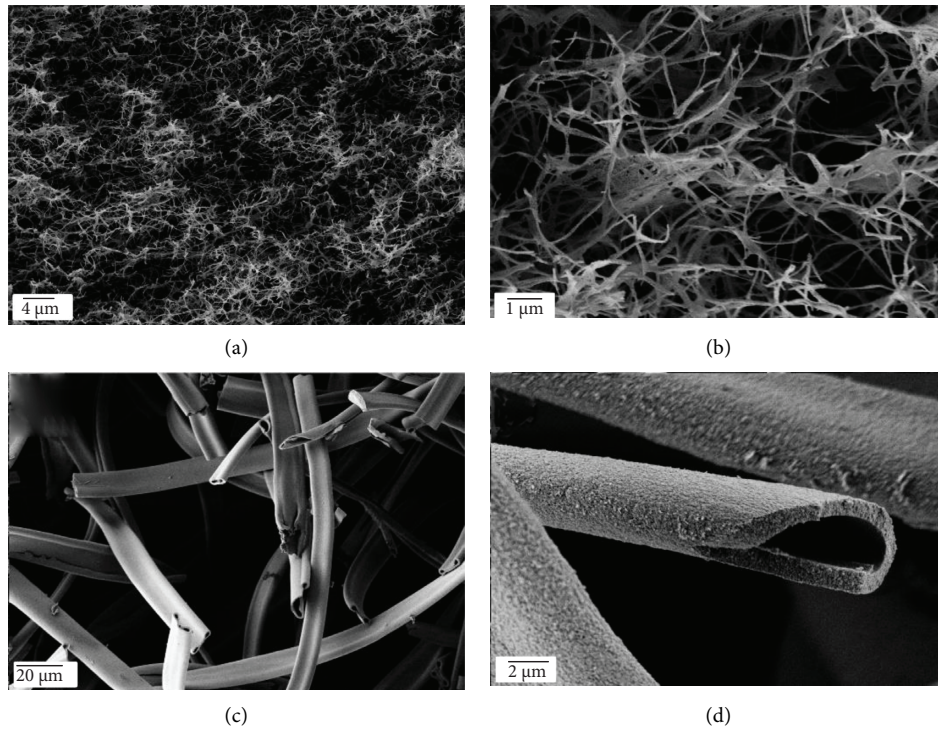
(a)

(b)

(c)

(d)

FIGURE 5: Structural morphology of TiO2 ALD-coated nanocellulose samples after pyrolysis (a) and (b). In (c) and (d), the morphology of TiO$_2$ coated Kynol samples after burnout in air, where a straw-like structure can be seen.
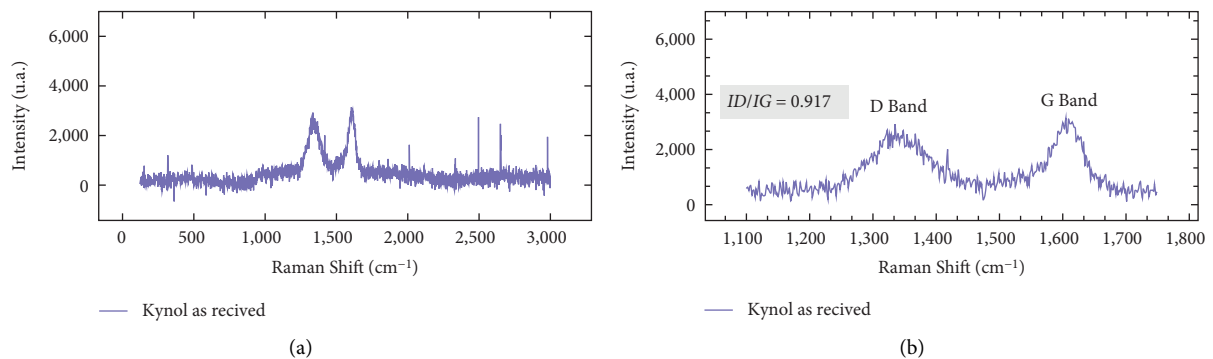

(a)

(b)

FIGURE 6: Kynol Raman spectroscopy in (a) and zoomed in (b) with D and G bands highlighted.

noncoated fiber. This hollow structure was expected since the heat treatment occurs in air and thus the carbon fraction was burned away, similar to the results found in [44]. Part of the thickness observed in Figure 5(d) may be extended by the gold sputtering.

3.3. Phase Identification and Evolution.
The Raman spectroscopy measurements of the Kynol samples prior to deposition (see Figure 6) show the expected carbon-related D and G bands at 1335 and 1604 cm^{-1}, respectively [46, 47]. The broad G band reveals the existence of more disordered carbon than the graphitic sheets present in the material. The ID/IG ratio, an indicator of the degree of disorder within a carbonaceous material [48, p. 202], we found was 0.917. This ratio is fairly close to what Lee found, 0.92, for another very

similar activated carbon textile from the same manufacturer [48]. This high ID/IG ratio is usually associated with high temperature processing, pyrolysis, but not graphitization [49].

The Kynol sample coated with TiO$_2$ ALD, Figure 7(d) and 7(e), shows a predominantly amorphous curve, with some peaks related to TiO$_2$ anatase phase peaks identified at 47.87°, 53.53°, and 54.86° (ICSD 009854). Broadbands centered around 23.92° and 24.57 °Correspond to carbon phases (ICSD 28417 and ICSD 28419) [50, 51]. A similar result has been found by Rahmawati et al. with a similar carbon substrate and TiO$_2$ deposition [52].

Meanwhile, the TiO$_2$ ALD-coated nanocellulose samples, Figures 7(a)–7(c), show peaks at 16.8° and 22.7°, corresponding to the typical profile of cellulose I polymorph (CCDC pattern number 1866391) [53]. However, in the
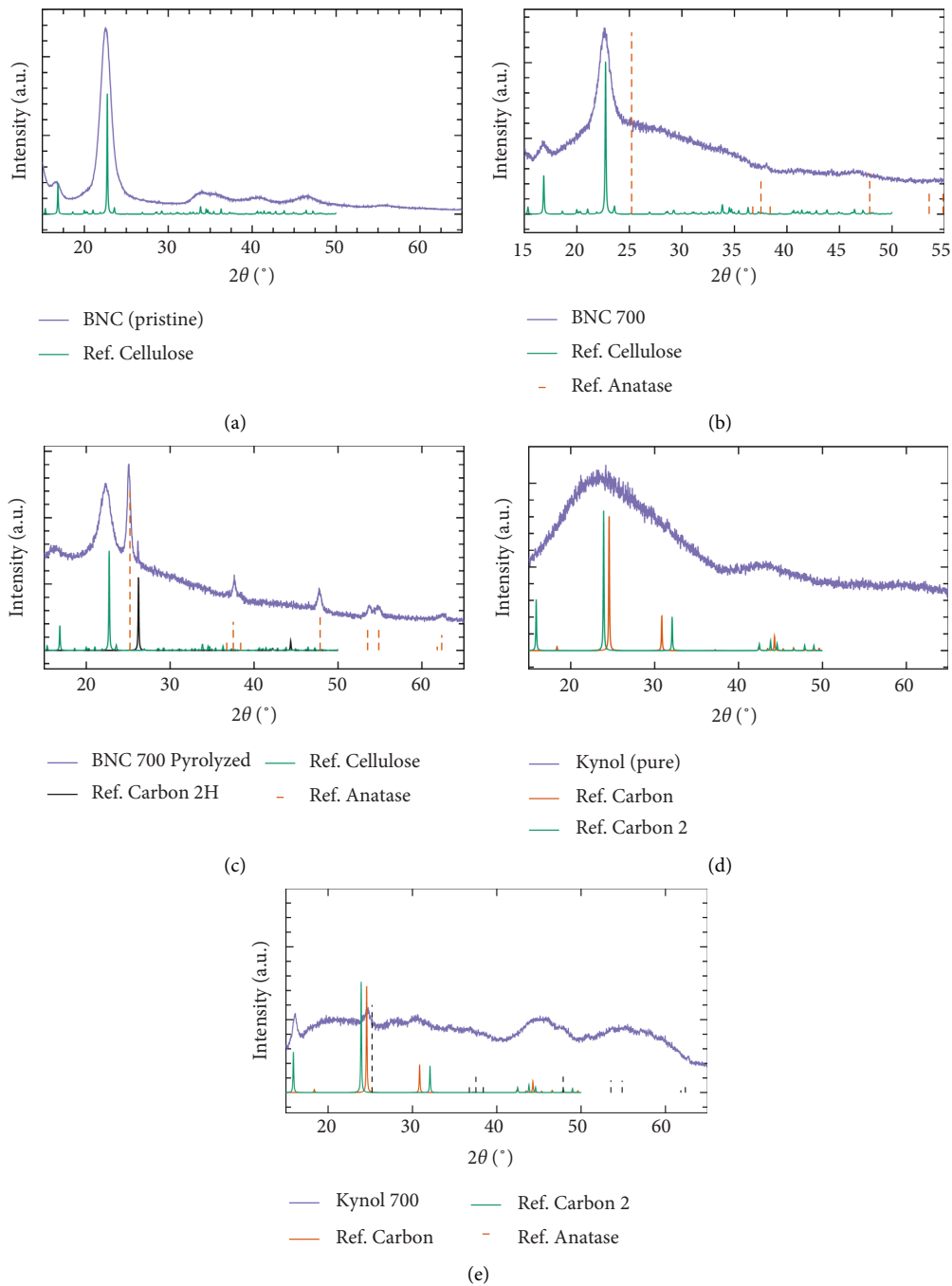
(a) (b)

(c) (d)

(e)

FIGURE 7: XRD patterns of (a) pristine BNC, (b) TiO_2 ALD-coated BNC, (c) ALD-coated BNC sample after pyrolysis, (d) pure Kynol, and (e) the TiO_2 ALD-coated Kynol.

pyrolyzed sample (Figure 7(c)), we see that the prominent peak remains despite the high temperature. We expected that they would have decreased [54]. This remaining peak suggests that the titania layer may have partially protected the fibers and partially graphitized them due to the appearance of the peaks at 26.2° and 44.3° (ICSD 31170). This result agrees with that published by Li et al. [55].

Finally, several anatase peaks were also identified at 25.2°, 37.5°, 53.53°, 54.86°, and 62.3°, and no rutile peaks could be detected. Refinement of the anatase phase, with a χ^2 value of

2.25 ($R^{wp} = 4.85\%$), which was considered acceptable according to [56], indicated a crystallite size of 80 ± 8 nm. The expected phase transition from anatase to rutile [57] did not occur, which could be a result of a confluence of factors such as crystallite size and particle size [58]. We believe that these factors are the most likely to have influenced our results. Crystallite size and particle size are directly related to the deposition temperature which has been shown to yield anatase after heat treatment at 900°C [59] and might have affected the grains. Henegar and Gougousi have demonstrated that it is

TABLE 2: Summary of anatase-stabilized titania sorted by annealing temperature.

| Synthesis Temp. (°C)	Annealing temp. (°C)	Crystallite size (nm)	Standard dev.	Remarks	Reference
23*	773	400	—	Iterative incipient wetness infiltration with intermediate drying at 160°C	[61]
95	800	80	8	BNC/Carbon template infi;ltrated with amorphous titania on low-temperature ALD	**This work**
100	900	200	—	Native oxide Si (100) deposited via ALD with TDMAT as a precursor	[60]
150	900	90	—	TiO$_2$ thin fi;lm deposited on Si (100) by remote plasma atomic layer deposition (RPALD)	[59]
95	1000	175	50	Polystyrene template infi;ltrated with amorphous titania using low-temperature ALD	[12]
23*	1000	—	—	Titanate nanowires deposited from a suspension via a stamping method	[62]

*Room temperature.
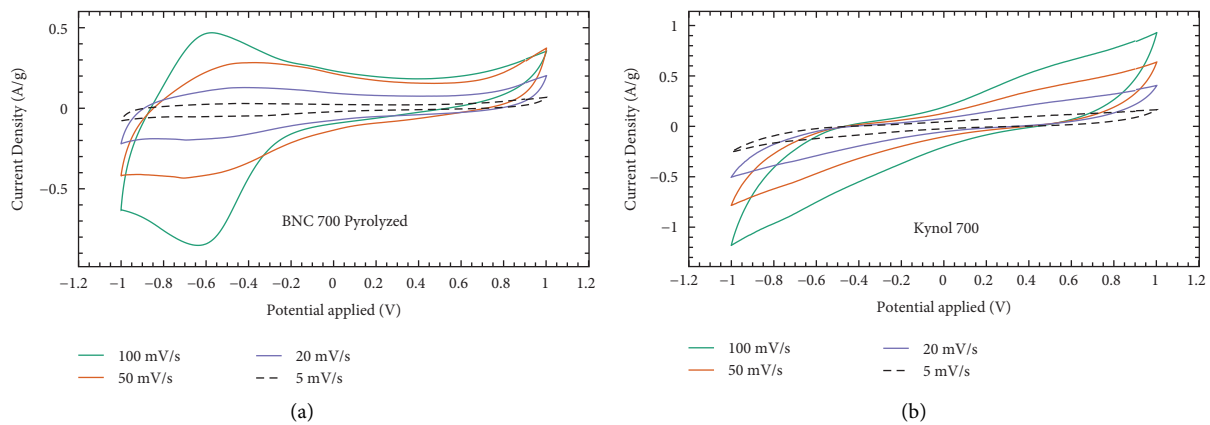
FIGURE 8: Cyclicvoltammetry on (a) the BNC 700 pyrolyzed sample with a more pseudocapacitance curve and on (b) Kynol 700.

possible to achieve anatase stabilization through ALD, even after annealing at 900°C, if the deposition temperature is below 150°C. They concluded that this is due to the crystallite size and the lower adhesion of the deposited layer to the substrate [60]. The ALD process in this work was set to 95°C, so the lower deposition temperature hypothesis is reasonable.

In addition to using a low deposition temperature, 95°C, Pasquarelli et al. have also demonstrated that an inverse opal substrate infiltrated via ALD can have its anatase-to-rutile transformation thermally delayed in air and inhibited under vacuum, even when heat treated at 1000°C for 4 h or 1300°C for 3 h under vacuum. They suggest that a highly porous structure could intrinsically hinder phase transformation by spatially limiting particle agglomeration and reducing the number of nucleation sites [12]. Other researchers have also investigated further and found similar results [61]. A short summary of those findings is presented in Table 2.

4. Nitrogen Adsorption

As expected, the specific surface area (SSA) decreased with the titania coating. Similar results have been observed for ALD-coated iron oxide nanoparticles [63]. Although the decrease is slight for the Kynol sample, from 1695 to 1480 m^2/g, it is considerable for the nanocellulose sample of 200 m^2/g (pristine from Ref. [64]) to 50 m^2/g. This small area indicates a potential non-optimal BNC structure, so that instead of individual fiber coating, severely agglomerated fibers are coated as a single piece of material [63]. The relatively lower area of the BNC could also be attributed to the structural deformation during manipulation and cutting. The increase in SSA for pyrolyzed nanocellulose, 175 m^2/g, is probably associated with fiber breakage and/or coating delamination, as observed in SEM images (Figure 5) and some loss of structure.

4.1. Electrochemical Characterization. Figure 8 shows the CVs of the samples at a specific gravimetric current density. The pyrolyzed BNC sample (Figure 8(a)) shows a more pseudo-capacitance curve. While the Kynol sample (Figure 8(b)) is much less pronounced and more symmetrical. The pyrolyzed BNC plot also suggests a less reversible process compared to that of the Kynol sample. As explained by Ntakirutimana and Tan, at the initial low scan rates (5 and 20 mV/s), the ions probably have time to completely diffuse into the porous structure, resulting in a greater contact between the electrolyte and the inner surface of the electrode, and by consequence, a larger capacitance [65]. However, at a higher scanning rate,
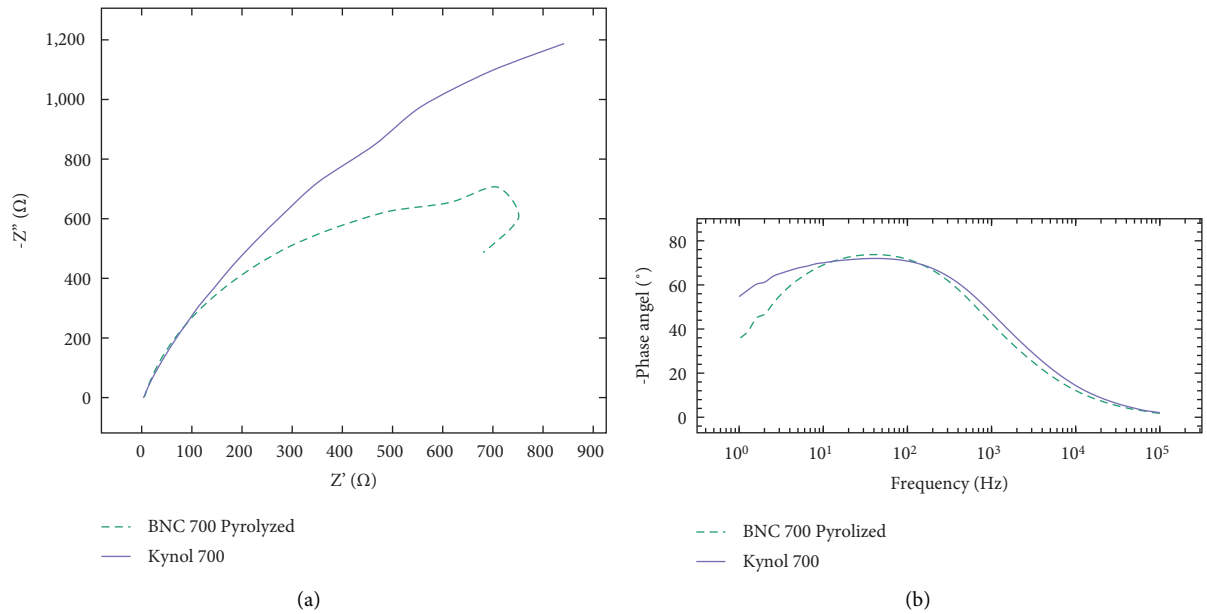
(a)

(b)

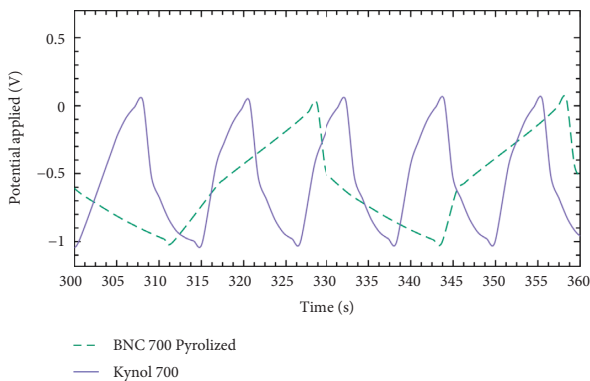FIGURE 9: In (a) Nyquist plot and in (b) Bode plot (100 kHz—1 Hz).

FIGURE 10: Galvanostatic charge-discharge over time.

there may not be enough time for complete diffusion of electrolyte ions and penetration of the charges into the internal structure of the electrode, which in turn results in a smaller capacitance [66].

The Nyquist plot is shown in Figure 9(a). The Kynol sample shows a distorted semicircular shape at all tested frequencies. It also shows that the BNC sample has decreased both the real and imaginary impedance at a higher frequency in an inductive loop. This change could be attributed to the diffusion difficulty at lower frequencies, which becomes less important as the frequency increases. The inductive loop, however, may be related to corrosion reactions at the electrode [67]. Impedance is also represented in the Bode plot in Figure 9(b), where all samples exhibited an almost ideal capacitor-like response.

The galvanostatic charge-discharge is plotted in Figure 10. The Kynol 700 shows an almost triangular profile of a supercapacitive charge storage. The pyrolyzed BNC 700 exhibited an asymmetrical profile, closer to a battery-like behavior, which is related to the layer thickness and textural structure.

TABLE 3: Specific capacitance at 5 mV/s compared to the specific surface area.

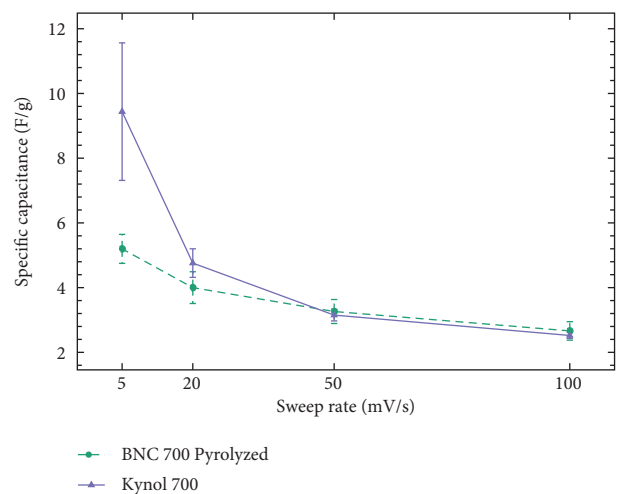| Sample	SSA (m^2/g)	Specific capacitance (F/g)
BNC 700 Py.	175.65	5.61
Kynol 700	1480.97	7.93

FIGURE 11: Specific capacitance versus sweep rate, from 5–100 mV/ s. The error bars represent the standard deviation of measurements for two runs on each sample ($n = 2$).

The specific capacitance, at 5 mV/s, shown in Table 3, suggests a positive correlation with the surface area. However, as seen in Figure 11, this relation does not hold as we increase the sweep rate. Figure 11 shows the relationship between the specific capacitance and the potential scanning rate. For both samples, it decreases the specific capacitance as the sweep rate increases. This could happen because with a slower scan, the electrolyte has more time to permeate
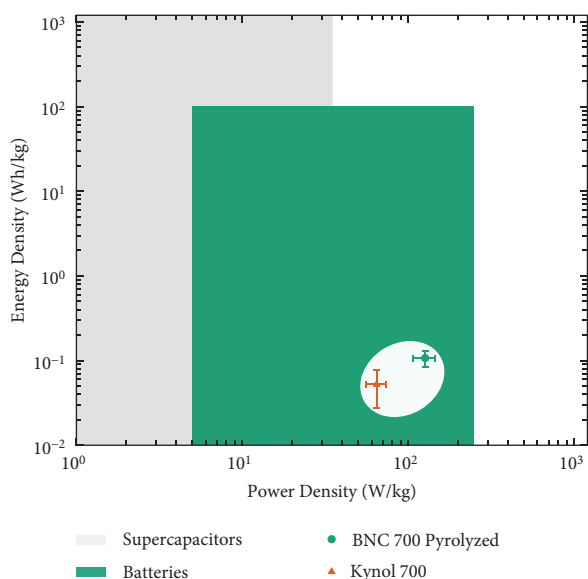
FIGURE 12: Ragone plot relating energy density with power density. The hatched green area corresponds to the usual battery limit and the hatched purple to supercapacitors. The error bars represent the standard deviation of measurements for four runs on each sample ($n = 4$).

deeper in between the fibers having a greater contact area with the surface of the electrode. This effect is more noticeable in the Kynol sample, probably due to the difference in macropore and fiber diameter (see Figure 5).

Figure 12 presents the Ragone plot, with specific capacitance. Both samples fit into the broad category of batteries with low energy density, which indicates that they are able to store a small amount of energy but are still capable of delivering this energy fast enough to be considered a battery.

5. Conclusions

In this way, BNC was coated with TiO_2 by ALD, and in a single heat-treatment step in the inert atmosphere, the BNC structure was pyrolyzed into carbon, and an anatase phase was obtained. Moreover, nonwoven carbon textiles were successfully coated with ALD while maintaining their surface area. The coating layer also maintains its shape and structure when the fiber is removed through burning, generating hollow titania fibers with a nanometric wall thickness. Additionally, when deposited at 95°C, titanium isopropoxide transformed into an anatase phase even after heat treatment at 800°C. Despite their relatively low capacitance, these properties could allow carbon fibrous coated with titania to be used in electrochemical energy storage devices once some parameters get fine-tuned. Variable parameters such as ALD thickness, pyrolysis temperature, electrolyte composition and concentration, and the weight proportion of the electrode assembly could be very useful for future work.

Data Availability

The data used to support the findings of this study are included within the article.

Conflicts of Interest

The authors declare that there are no conflicts of interest regarding the publication of this paper.

Acknowledgments

References

[1] S. M. George, "Atomic layer deposition: an overview," *Chemistry Review*, vol. 110, no. 1, pp. 111–131, Jan. 2010.

[2] R. W. Johnson, A. Hultqvist, and S. F. Bent, "A brief review of atomic layer deposition: from fundamentals to applications," *Materials Today*, vol. 17, no. 5, pp. 236–246, Jun. 2014.

[3] N. Aluru, A. Beskok, and G. Karniadakis, *Microflows and Nanoflows*, Springer, New York, NY, USA, 2005.

[4] E. Ahvenniemi, A. R. Akbashev, S. Ali et al., "Review Article: recommended reading list of early publications on atomic layer deposition—outcome of the 'Virtual Project on the History of ALD," *Journal of Vacuum Science and Technology A: Vacuum, Surfaces, and Films*, vol. 35, no. 1, p. 010801, 2017.

[5] M. M. Rashid, B. Simončič, and B. Tomšič, "Recent advances in TiO2-functionalized textile surfaces," *Surfaces and Interfaces*, vol. 22, p. 100890, 2021.

[6] M. Kemell, V. Pore, M. Ritala, M. Leskelä, and M. Lindén, "Atomic layer deposition in nanometer-level replication of cellulosic substances and preparation of photocatalytic TiO2/cellulose composites," *Journal of the American Chemical Society*, vol. 127, no. 41, pp. 14178-14179, 2005.

[7] H. I. Akyildiz, S. Diler, and S. Islam, "Evaluation of TiO2 and ZnO atomic layer deposition coated polyamide 66 fabrics for photocatalytic activity and antibacterial applications," *Journal of Vacuum Science & Technology A*, vol. 39, no. 2, p. 022405, 2021.

[8] Y. Li, J. P. Wooding, E. K. McGuinness, Y. Sun, and M. D. Losego, "Thermally stimulated wettability transformations on one-cycle atomic layer deposition-coated cellulosic paper: applications for droplet manipulation and heat patterned paper fluidics," *ACS Applied Materials & Interfaces*, vol. 13, no. 11, pp. 13802–13812, 2021.

[9] C. Militzer, P. Dill, and W. A. Goedel, "Atomic layer deposition onto carbon fiber fabrics," *J. Am. Ceram. Soc.* vol. 100, no. 12, pp. 5409–5420, 2017.

[10] K. P. Furlan, R. M. Pasquarelli, T. Krekeler et al., "Highly porous α-Al2O3 ceramics obtained by sintering atomic layer deposited inverse opals," *Ceramics International*, vol. 43, no. 14, pp. 11260–11264, 2017.

[11] S. Zhu, J. Liu, and J. Sun, "Growth of ultrathin SnO2 on carbon nanotubes by atomic layer deposition and their application in lithium ion battery anodes," *Applied Surface Science*, vol. 484, pp. 600–609, Aug. 2019.

[12] R. M. Pasquarelli, H. S. Lee, R. Kubrin et al., "Enhanced structural and phase stability of titania inverse opals," *Journal of the European Ceramic Society*, vol. 35, no. 11, pp. 3103–3109, 2015.

[13] G. P. Gakis, C. Vahlas, H. Vergnes et al., "Investigation of the initial deposition steps and the interfacial layer of Atomic Layer Deposited (ALD) Al2O3 on Si," *Applied Surface Science*, vol. 492, pp. 245–254, Oct. 2019.

[14] Y.-Q. Cao, S.-S. Wang, C. Liu, D. Wu, and A.-D. Li, "Atomic layer deposition of ZnO/TiO2 nanolaminates as ultra-long life anode material for lithium-ion batteries," *Sci. Rep.*vol. 9, no. 1, p. 11526, 2019.

[15] Y. Q. Cao, T. Q. Zi, X. R. Zhao et al., "Enhanced visible light photocatalytic activity of Fe2O3 modified TiO2 prepared by atomic layer deposition," *Sci. Rep.*vol. 10, no. 1, p. 13437, 2020.

[16] M. Trought, I. Wentworth, C. de Alwis, T. R. Leftwich, and K. A. Perrine, "Influence of surface etching and oxidation on the morphological growth of Al2O3 by ALD," *Surface Science*, vol. 690, p. 121479, 2019.

[17] S. An, B. Joshi, A. L. Yarin, M. T. Swihart, and S. S. Yoon, "Supersonic cold spraying for energy and environmental applications: one-step scalable coating Technology for advanced micro- and nanotextured materials," *Advanced Materials*, vol. 32, no. 2, p. 1905028, 2019.

[18] G. Darwish, S. Huang, K. Knoernschild et al., "Improving polymethyl methacrylate resin using a novel titanium dioxide coating," *Journal of Prosthodontics*, vol. 28, no. 9, pp. 1011–1017, 2019.

[19] M. Iguchi, S. Yamanaka, and A. Budhiono, "Bacterial cellulose — a masterpiece of nature's arts," *Journal of Materials Science*, vol. 35, no. 2, pp. 261–270, 2000.

[20] F. G. Blanco Parte, S. P. Santoso, C. C. Chou et al., "Current progress on the production, modification, and applications of bacterial cellulose," *Critical Reviews in Biotechnology*, vol. 40, no. 3, pp. 397–414, Jan. 2020.

[21] P. A. Rühs, F. Storz, G. O. Loo, M. Haug, and P. Fischer, "3D bacterial cellulose biofilms formed by foam templating," *Npj Biofilms Microbiomes*, vol. 4, no. 1, p. 21, 2018.

[22] S. Swingler, A. Gupta, H. Gibson, M. Kowalczuk, W. Heaselgrave, and I. Radecka, "Recent advances and applications of bacterial cellulose in biomedicine," *Polymers*, vol. 13, no. 3, p. 412, 2021.

[23] L. M. Cavalcanti, F. C. M. Pinto, G. M. D. Oliveira, S. V. C. Lima, J. L. D. A. Aguiar, and E. M. Lins, "Efficacy of bacterial cellulose membrane for the treatment of lower limbs chronic varicose ulcers: a randomized and controlled trial," *Revista do Colégio Brasileiro de Cirurgiões*, vol. 44, no. 1, pp. 72–80, 2017.

[24] J. Kim, S. W. Kim, S. Park et al., "Bacterial cellulose nanofibrillar patch as a wound healing platform of tympanic membrane perforation," *Advanced Healthcare Materials*, vol. 2, no. 11, pp. 1525–1531, 2013.

[25] M. Gao, J. Li, Z. Bao et al., "A natural in situ fabrication method of functional bacterial cellulose using a microorganism," *Nat Commun*, vol. 10, no. 1, p. 437, 2019.

[26] M. N. F. Norrrahim, N. A. Mohd Kasim, V. F. Knight et al., "Nanocellulose: the next super versatile material for the military," *Materials Advances*, vol. 2, no. 5, pp. 1485–1506, 2021.

[27] J. S. Hayes, "Nanostructure of activated carbon fibers and kinetics of adsorption/desorption," in *Air & Waste Management Association Annual Conference and Exhibition*, vol. 43052, pp. 689–710, United States, Jul, Baltimore, MD, 2002.

[28] N. C. Ellebracht and C. W. Jones, "Amine functionalization of cellulose nanocrystals for acid–base organocatalysis: surface chemistry, cross-linking, and solvent effects," *Cellulose*, vol. 25, no. 11, pp. 6495–6512, 2018.

[29] Y. Habibi, "Key advances in the chemical modification of nanocelluloses," *Chem. Soc. Rev.*vol. 43, no. 5, pp. 1519–1542, 2014.

[30] H. Liu, B. Geng, Y. Chen, and H. Wang, "Review on the aerogel-type oil sorbents derived from nanocellulose," *ACS Sustainable Chemistry & Engineering*, vol. 5, no. 1, pp. 49–66, 2016.

[31] V. V. Revin, A. V. Dolganov, E. V. Liyaskina et al., "Characterizing bacterial cellulose produced byKomagataeibacter sucrofermentans H-110 on molasses medium and obtaining a biocomposite based on it for the adsorption of fluoride," *Polymers*, vol. 13, no. 9, p. 1422, 2021.

[32] E. by F. Béguin and E. zbieta Frąckowiak, Eds., *Supercapacitors: Materials, Systems, and Applications*, Wiley VCH, 2013.

[33] P. Simon and Y. Gogotsi, "Materials for electrochemical capacitors," in *Nanoscience and Technology*, pp. 320–329, Co-Published with Macmillan Publishers Ltd, UK, 2009.

[34] Y. Jiang, Z. Wang, C. Xu et al., "Atomic layer deposition for improved lithiophilicity and solid electrolyte interface stability during lithium plating," *Energy Storage Materials*, vol. 28, pp. 17–26, Jun. 2020.

[35] J. T. Korhonen, P. Hiekkataipale, J. Malm, M. Karppinen, O. Ikkala, and R. H. A. Ras, "Inorganic hollow nanotube Aerogels by atomic layer deposition onto native nanocellulose templates," *ACS Nano*, vol. 5, no. 3, p. 1974, 2011.

[36] L. Ma, R. Liu, H. Niu, L. Xing, L. Liu, and Y. Huang, "Flexible and freestanding supercapacitor electrodes based on nitrogen-doped carbon networks/graphene/bacterial cellulose with ultrahigh areal capacitance," *ACS Applied Materials & Interfaces*, vol. 8, no. 49, pp. 33608–33618, 2016.

[37] K. Cesca, M. Schadeck Netto, V. Lunkes Ely, G. L. Dotto, E. L. Foletto, and D. Hotza, "Synthesis of spherical bacterial nanocellulose as a potential silver adsorption agent for antimicrobial purposes," *Cellulose Chemistry And Technology*, vol. 54, no. 3–4, pp. 285–290, 2020.

[38] J. Lim, S. Y. Ryu, J. Kim, and Y. Jun, "A study of TiO2/carbon black composition as counter electrode materials for dye-sensitized solar cells," *Nanoscale Res. Lett.*vol. 8, no. 1, p. 227, May 2013.

[39] W.-J. Lee, Y.-T. Wu, Y.-W. Liao, and Y.-T. Liu, "Graphite felt modified by atomic layer deposition with TiO2 nanocoating exhibits super-hydrophilicity, low charge-transform resistance, and high electrochemical activity," *Nanomaterials*, vol. 10, no. 9, p. 1710, 2020.

[40] A. Altomare, N. Corriero, C. Cuocci, A. Falcicchio, A. Moliterni, and R. Rizzi, "QUALX2.0: a qualitative phase analysis software using the freely available database POW_COD," *Journal of Applied Crystallography*, vol. 48, no. 2, pp. 598–603, Feb. 2015.

[41] N. Doebelin and R. Kleeberg, "Profex: a graphical user interface for the Rietveld refinement programBGMN," *Journal of Applied Crystallography*, vol. 48, no. 5, pp. 1573–1580, 2015.

[42] E. V. Skopin, K. Abdukayumov, P. Abi Younes et al., "In situ ellipsometry monitoring of TiO2 atomic layer deposition from Tetrakis(dimethylamido)titanium(IV) and H2O precursors on Si and In0.53Ga0.47As substrates," *Thin Solid Films*, vol. 723, no. 8, p. 138591, 2021.

[43] C. Chen, M. Mo, W. Chen et al., "Highly conductive nano-composites based on cellulose nanofiber networks via NaOH treatments," *Composites Science and Technology*, vol. 156, pp. 103–108, 2018.

[44] W. Lee, *Overcoming Parasitic Reactions Occurring in Carbonaceous Seawater Battery Cathodes and Their Mechanisms,"* *Mathesis*, Ulsan National Institute of Science and Technology, South Korea, 2021, https://scholarworks.unist.ac.kr/handle/201301/50439.

[45] W. Waleczek, J. Dendooven, P. Dyachenko et al., "Influence of alumina addition on the optical properties and the thermal stability of titania thin films and inverse opals produced by atomic layer deposition," *Nanomaterials*, vol. 11, no. 4, p. 1053, 2021.

[46] C. Castiglioni, C. Mapelli, F. Negri, and G. Zerbi, "Origin of the D line in the Raman spectrum of graphite: a study based on Raman frequencies and intensities of polycyclic aromatic hydrocarbon molecules," *J. Chem. Phys.* vol. 114, no. 2, p. 963, 2001.

[47] R. J. K. S. C. E. Borowiak-palen, M. Kruszyńska, and A. Bachmatiuk, "Characterization of carbon nanotubes by Raman spectroscopy," *Mater. Sci.-Pol.* vol. 26, no. 2, pp. 433–441, 2008.

[48] R. S. G. Dresselhaus and M. S. Dresselhau, "Physical properties of carbon nanotubes," *World Scientific Publishing Company*, vol. 897, p. 4890, 1998.

[49] A. C. Ferrari and J. Robertson, "Interpretation of Raman spectra of disordered and amorphous carbon," *Physical Review B*, vol. 61, no. 20, pp. 14095–14107, May 2000.

[50] M. Salahuddin, M. N. Uddin, G. Hwang, and R. Asmatulu, "Superhydrophobic PAN nanofibers for gas diffusion layers of proton exchange membrane fuel cells for cathodic water management," *International Journal of Hydrogen Energy*, vol. 43, no. 25, pp. 11530–11538, 2018.

[51] B. Liu, S. Liu, Z. He et al., "Improving the performance of negative electrode for vanadium redox flow battery by decorating bismuth hydrogen edetate complex on carbon felt," *Ionics*, vol. 25, no. 9, pp. 4231–4241, May 2019.

[52] F. Rahmawati, F. R. Putri, and A. Masykur, "The photocatalytic activity of zns-TiO2 on a carbon fiber prepared by chemical bath deposition," *Open Chemistry*, vol. 17, no. 1, pp. 132–141, Apr. 2019.

[53] E. Tsouko, C. Kourmentza, D. Ladakis et al., "Bacterial cellulose production from industrial waste and by-product streams," *International Journal of Molecular Sciences*, vol. 16, no. 12, pp. 14832–14849, 2015.

[54] J. Liang, J. Chen, S. Wu, C. Liu, and M. Lei, "Comprehensive insights into cellulose structure evolution via multi-perspective analysis during a slow pyrolysis process," *Sustainable Energy & Fuels*, vol. 2, no. 8, pp. 1855–1862, 2018.

[55] S. Li, J. Warzywoda, S. Wang, G. Ren, and Z. Fan, "Bacterial cellulose derived carbon nanofiber aerogel with lithium polysulfide catholyte for lithium–sulfur batteries," *Carbon*, vol. 124, pp. 212–218, Nov. 2017.

[56] B. H. Toby, "R factors in Rietveld analysis: how good is good enough?" *Powder Diffraction*, vol. 21, no. 1, pp. 67–70, 2006.

[57] F. A. Scaramuzzo, A. Dell'Era, G. Tarquini, R. Caminiti, P. Ballirano, and M. Pasquali, "Phase transition of TiO_2 nanotubes: an X-ray study as a function of temperature," *The Journal of Physical Chemistry C*, vol. 121, no. 44, pp. 24871–24876, 2017.

[58] D. A. H. Hanaor and C. C. Sorrell, "Review of the anatase to rutile phase transformation," *Journal of Materials Science*, vol. 46, no. 4, pp. 855–874, 2017.

[59] J. Lee, S. J. Lee, W. B. Han et al., "Deposition temperature dependence of titanium oxide thin films grown by remote-plasma atomic layer deposition," *Physica Status Solidi (A)*, vol. 210, no. 2, pp. 276–284, Oct. 2012.

[60] A. J. Henegar and T. Gougousi, "Stability and surface reactivity of anatase TiO2 films," *ECS Journal of Solid State Science and Technology*, vol. 4, no. 8, pp. P298–P304, 2015.

[61] D. G. Gregory, Q. Guo, L. Lu, C. J. Kiely, and M. A. Snyder, "Template-induced structuring and tunable polymorphism of three-dimensionally ordered mesoporous (3DOm) metal oxides," *Langmuir*, vol. 33, no. 26, pp. 6601–6610, 2017.

[62] L. Rossi, X. Berdat, M. Spina et al., "Thermal coarsening of individual titanate nanowires and their assemblies: surface vs. bulk diffusion," *Ceramics International*, vol. 46, no. 10, pp. 16321–16327, 2020.

[63] C.-L. Duan, Z. Deng, K. Cao, H.-F. Yin, B. Shan, and R. Chen, "Surface passivation of Fe3O4 nanoparticles with Al2O3 via atomic layer deposition in a rotating fluidized bed reactor," *Journal of Vacuum Science & Technology A: Vacuum, Surfaces, and Films*, vol. 34, no. 4, p. 04C103, 2016.

[64] F. Liebner, E. Haimer, M. Wendland et al., "Aerogels from unaltered bacterial cellulose: application of scCO2 drying for the preparation of shaped, ultra-lightweight cellulosic aerogels," *Macromol. Biosci.* vol. 10, no. 4, pp. 349–352, Feb. 2010.

[65] H.-Y. Liu, K.-P. Wang, and H. Teng, "A simplified preparation of mesoporous carbon and the examination of the carbon accessibility for electric double layer formation," *Carbon*, vol. 43, no. 3, pp. 559–566, 2005.

[66] S. Ntakirutimana and W. Tan, "Electrochemical capacitive behaviors of carbon/titania composite prepared by Tween 80-assisted sol-gel process for capacitive deionization," *Desalination*, vol. 512, p. 115131, 2021.

[67] K.-C. Pham, D. S. McPhail, C. Mattevi, A. T. S. Wee, and D. H. C. Chua, "Graphene-carbon nanotube hybrids as robust catalyst supports in proton exchange membrane fuel cells," *J. Electrochem. Soc.,* vol. 163, no. 3, pp. F255–F263, 2016.